Plasmonic hybrid core-shell (HyCoS) AgPt NP template hybridized with GQDs for SERS enhancement of 4-MBA and BT

Kunwar, Sundar

To be published in: Journal of Alloys and Compounds

DOI to publisher's version: 10.1016/j.jallcom.2023.169952

Plasmonic hybrid core-shell (HyCoS) AgPt NP template hybridized with GQDs for SERS enhancement of 4-MBA and BT

Shusen Lin[1], Md Ahasan Habib[1], Shalmali Burse[1], Rutuja Mandavkar[1], Mehedi Hasan Joni[1], Sundar Kunwar[1,2*] and Jihoon Lee[1**]

[1] Department of Electronic Engineering, College of Electronics and Information, Kwangwoon University, Nowon-gu, Seoul, 01897, South Korea.

[2] Center for Integrated Nanotechnologies (CINT), Los Alamos National Laboratory, Los Alamos, New Mexico 87545, USA

Correspondence e-mail: sundar@lanl.gov (S. Kunwar)*, jihoonlee@kw.ac.kr (J. Lee)**

Abstract: Surface-enhanced Raman spectroscopy (SERS) is an attractive vibrational spectroscopic technique that can enable a non-destructive and ultra-sensitive detection down to the single-molecule level. Herein, a novel hybrid SERS platform is developed based on hybrid core-shell (HyCoS) AgPt nanoparticles (NPs) and graphene quantum dots (GQDs) for the enhancement of Raman vibration of 4-mercaptobenzoic acid (4-MBA) and benzenethiol (BT). The unique design of HyCoS AgPt NPs induces strong electromagnetic mechanism (EM) enhancement through the amplification of electromagnetic fields by the excitation of high-density surface plasmons and hot spots. Superior localized surface plasmon resonance (LSPR) is generated by the AgPt core-shell and background Ag NP coupling, which is systematically investigated by the optical properties and FDTD simulations. The background Ag NPs can further increase the coverage of metallic NPs, leading to higher-density hot spots and enhanced SERS response. At the same time, GQDs can provide plentiful accessible edges for the charge transfer to the HOMO and LUMO of 4-MBA and BT based on the chemical mechanism (CM) enhancement. The mixing approach of GQDs and target molecules on the HyCoS

AgPt NPs can significantly amplify the Raman signals via the strong adsorption of probe molecules by the $\pi - \pi$ interaction. The enhancement factors of proposed SERS platform can reach ~10^7 and ~10^5 for the 4-MBA and BT respectively.

Keywords: HyCoS AgPt NPs, localized surface plasmon resonance (LSPR), GQDs, chemical mechanism (CM), electromagnetic mechanism (EM)

1. Introduction

Surface-enhanced Raman spectroscopy (SERS) is a surface-sensitive technique that can significantly amplify the Raman signals by orders of magnitude for the molecules adsorbed on the specific platform [1–3]. It has the advantages of rapid, in-situ, non-destructive molecular identification, resulting in a wide range of applications in catalysis, biosensing and environmental science [4–6]. Up to now, the dominant contributor to the SERS effect is the electromagnetic mechanism (EM) enhancement, which is ascribed by the amplification of local electromagnetic field and hot spot generation based on the localized surface plasmon resonance (LSPR) [7,8]. The LSPR properties are strongly dependent on the NP elements and dimensional factors such as size, density and configuration [9,10]. The classic plasmonic substrates incorporating Au, Ag and Cu nanoparticles (NPs) have been extensively studied and various configurations with other material decorations have also been widely explored for the SERS enhancement such as Au@Cu_2O–Ag composite [11], Au nanowires [12], Au/Ag core-shell [13], $CoTiO_3$@Ag nanofibers [14] and so forth. Ag-based substrate exhibit higher SERS enhancement over the Au and Cu due to its inherent strong plasmonic properties [9,10,15]. Meanwhile, Pt NPs are relatively rarely investigated for the SERS substrate. The Pt NPs can still demonstrate strong excitation of surface plasmons with excellent chemical stability, which can make it suitable as plasmonic SERS template [16]. Therefore, combining Pt and Ag together in a hybrid SERS platform can be a useful strategy to improve the Raman signal of

probe molecules and enhance the functionality of SERS application.

In the meantime, the chemical mechanism (CM) also plays an important role in SERS, which involves the charge transfer between the substrate and probe molecules through the molecular resonance and interfacial non-resonant interactions [17]. The CM is generally considered as a short-range effect as compared with the EM, which is dependent on the chemical structures, interactions and vibration modes [18]. Recently, novel semiconductor materials such MoS_2, TiO_2, ZnO, and graphene quantum dots (GQDs) have been reported to demonstrate strong CM enhancements due to their superior charge transfer capabilities. Among them, the GQDs as a zero-dimensional semiconductor structure can demonstrate outstanding chemical and physical properties such as good photoluminescence, biocompatibility, high accessibility and surface functionalization, which makes it an appealing candidate for the SERS [19,20]. The hydrogen-terminated edges and bonds in GQDs may promote the efficient charge transfer to the highest occupied molecular orbital (HOMO) and lowest unoccupied molecular orbital (LUMO) levels of probe molecules and enable the enhancement of Raman signals [21]. For instance, Zou et. al reported the Fe_3O_4-Au-GQDs SERS platform, exhibiting excellent sensitivity for the detection of protein [22]. Jin et. al demonstrated the core-shell structured Ag/o-GQD substrate for the H_2O_2 sensing down to the subcellular level due to a highly-efficient charge transfer as well as EM [23]. To this end, an innovative SERS platform based on the integration of GQD with hybrid AgPt NPs can serve as a promising candidate for the enhancement of SERS signals.

In this work, a hybrid SERS platform incorporating AgPt hybrid core-shell (HyCoS) NPs and GQD for the enhancement of 4-MBA and BT Raman signals has been successfully demonstrated by combining the CM and EM effects together as seen in Fig. 1(a). The CM enhancement is achieved by mixing GQDs with the probe molecules to enhance the charge transfer from GQD to the HOMO and LUMO levels of 4-MBA and BT as shown in Fig. 1(b). The HyCoS AgPt NPs can provide abundant hot spots and strong local electromagnetic fields by the strong LSPR, which can

significantly amplify the Raman signals based on the EM enhancement as shown in Fig. 1(c). The plasmonic HyCoS AgPt NP template is prepared by a two-step solid-state dewetting (SSD) process as shown in Fig. 1(d). The optimal NPs template is obtained by varying the Ag coating thickness and annealing temperature. According to the morphological and optical analysis, the Pt NPs template with 10 nm Ag coating annealed at 600 ºC is found to demonstrate the best SERS template. The finite-difference time-domain (FDTD) simulation also is performed to further analyze the distribution of local electromagnetic fields of various metallic NP configurations. The hybrid design based on the HyCoS AgPt NPs and GQD by utilizing both CM and EM can offer a great potential for the SERS application.

2. Experimental section

2.1. Preparation of Pt NPs:

A 20 nm-thick Pt layer was deposited on the prepared sapphires in a plasma-assisted sputtering chamber using Pt metal targets of 99.999% purity. The base pressure and ionization currents were 1 × 10^{-1} torr and 3 mA respectively, indicating a deposition rate of 0.05 nm s^{-1}. Subsequently, the deposited samples were mounted in the PLD chamber and the first-step solid-state dewetting process (SSD) was carried out at 800 °C for 450 s to fabricate dome shape Pt NP template [24]. The base pressure in PLD chamber was below 1 × 10^{-4} torr and the temperature ramping rate was 4 °C/s. The surface morphology of Pt NP template is shown in Fig. S2. Details on the substrate preparation can be found in the supplementary section S-1.

2.2. Preparation of various AgPt NPs:

The as-prepared Pt NP templates were sputtered with the 5, 10 and 20 nm Ag films respectively by using Ag metal targets with the purity of 99.999%. The second step SSD was performed in PLD chamber at various target annealing temperatures such as 400 and 600 °C for 120 s to fabricate

various metallic AgPt NPs. The growth process was terminated by turning off the heating system and the AgPt NPs were taken out after cooling down to room temperature. The surface morphology, reflectance, and transmittance of different thicknesses of Ag films are presented in Fig. S3. Details on the morphological and elemental characterizations can be found in the supplementary section S-2.

2.3. SERS solution preparation

4-mercaptobenzoic acid (4-MBA, Sigma Aldrich) and benzenethiol (BT, Sigma Aldrich) were dissolved in ethanol to prepare the stock solution with a molarity of 10^{-3} M. The stock solution was further diluted to prepare various molarity of 4-MBA and BT solutions from 10^{-4} to 10^{-7} M. The graphene quantum dots (GQDs) solution was prepared by dissolving 0.25 mg of GQD powder (Sigma Aldrich) in 1 ml of absolute ethanol (Sigma Aldrich). The average diameter of GQD was less than 5 nm. The GQD solution was used as a mixture (1:1, 2:1; 10:1) with the 4-MBA or BT molecules. 20 µl of different molarity or mixture solutions were drop-cast on the various substrates to measure the SERS signals. The SERS enhancement factor (EF) calculation can be found in the supplementary section S-4 and relative standard deviation (RSD) calculation is provided in S-5.

3. Results and discussion

3.1 Fabrication of hybrid core-shell (HyCoS) AgPt nanoparticles (NPs)

Figure 2 shows the hybrid core-shell (HyCoS) AgPt nanoparticles (NPs) with 10 nm Ag coatings on the Pt NPs templates at different annealing temperatures. To begin with, the Pt templates with the well-separated Pt NPs were formed by the 1st step solid-state dewetting (SSD) process via annealing 20 nm Pt thin film at 800 °C for 450 s. Generally, the optimum dewetting temperature for realizing desired metallic NPs should be close to the Tammann temperature (T_{Tammann}), at which the atoms start to diffuse in the bulk phase [25,26]. The T_{Tammann} is approximately equal to the half of melting point (T_{melting}) of metallic elements. The $T_{\text{melting Pt}}$ is 1768 ℃ and thus 800 °C was adapted for the 1st

step SSD [27]. In this regard, the agglomeration process along with the void nucleation occurred in the vicinity of ruptures and grain boundaries due to the surface and interface energy minimization [8,28]. As a result, the droplet-like Pt NPs were formed as seen in Fig. S2, exhibiting the average height and diameter of ~ 45 and ~ 160 nm. Then, the AgPt NPs were formed in the 2nd step SSD process after 10 nm Ag coating. The AFM image of Ag-coated Pt NPs without annealing is shown in Fig. 2(a), which demonstrated no apparent change in size and shape as seen in the corresponding line-profile in Fig. 2(a-1). The scanning of background (BG) surface where it is in between the Ag-coated Pt NPs is shown in Figs. 2(a-2) – 2(a-3). The uneven background surface can indicate an abundance of point defects and inhomogeneities such as voids, triple junctions and grain boundaries [8]. It can be also observed by directly coating Ag layer on bare sapphire as seen in Fig. S3. Initiated by the thermal annealing, the Ag adatoms started to diffuse toward the high chemical potential sites such as Pt NPs, resulting in the Pt core-Ag shell structure through the thermal energy-driven atomic dewetting process [8,29]. Meanwhile, the Ag adatoms can also dewet in the background, involving the rupture of thin films and diffusion of adatoms, resulting in the formation of secondary background (BG) Ag NPs [10]. The high-density background Ag NPs surrounded the core-shell NPs and the whole structure is indicated as a hybrid core-shell (HyCoS) AgPt NP configuration. The temperature-dependent surface morphology evolution is shown in Figs. 2(b) – 2(c). Here, the primary Pt NPs were well retained regardless of the annealing temperature and the BG Ag NPs were also gradually evolved. With the detailed analysis of line profiles, the average height and diameter of core-shell NP was gradually decreased at increased temperature as seen in Figs. 2(b-1) – 2(c-1) and Fig. 2(d). This can be explained by the BG NP development with the enhanced surface diffusion at increased temperature [8]. The size of secondary Ag NPs was increased at increased temperature as seen in Figs. 2(b-3) – 2(c-3) since the formed BG NPs tended to absorb nearby adatoms and can grow further [9]. The absorption boundary can be increased with the increased temperature. Additional AFM images of HyCoS AgPt NPs coated with 10 nm Ag can be seen in Fig. S4. The trend of

morphological changes can be expressed in terms of the Rq and SAR plots as seen in Figs. 2(e) – 2(f). The Rq represents the average surface height, described by the relation $Rq = \sqrt{\left(\frac{1}{n}\sum_1^n H_n^2\right)}$, where H_n is the profile height at each pixel. The SAR is determined by the measure of 3D surface area (A_s) concerning the geometric area (A_g) by the relation $\text{SAR} = \frac{\text{Ag} - \text{As}}{\text{Ag}} \times 100\ \%$ [8–10]. In this set, although the BG Ag NP was developing, the size reduction of primary NPs was more significant and thus the Rq and SAR both exhibited a gradually decreased trend. The atomic percentage of Pt and Ag element of this set was summarized in Fig. 2(g) based on the corresponding full range EDS spectra in Fig. S5. The atomic percentage change at incased temperature can be due to the Ag sublimation with increased vapor pressure [10, 30]. The EDS phase maps of HyCoS AgPt at 600 ºC are shown in Fig. 2(h) – 2(h-3). The phase maps of Pt Mα1 and SEM image were matched well, indicating well retained primary Pt NPs at the original Pt NP sites. Then, the Ag Lα1 map showed the Ag counts everywhere with the Ag higher counts at the core-shell AgPt NP sites, likely due to the formation of BG Ag NPs and higher Ag diffusion toward the Pt NP sites. The Al Kα phase was from the sapphire substrate (Al_2O_3). The fabrication of HyCoS AgPt NPs with a thinner 5 nm Ag layer was further conducted and morphological characterizations are shown in Figs. S6 – S8. The 5 nm set demonstrated a similar evolution trend to the 10 nm Ag set. However, the BG Ag NPs were smaller due to the thinner Ag thickness. Additional experiments with the 20-nm Ag layer were also conducted as seen in Figs. S10 – S13, which demonstrated totally different evolution trend. As discussed, the Pt NP sites possess higher chemical potentials (or lower surface energy) and thus the Ag adatoms will diffuse toward the Pt NPs upon annealing [31]. However, the increased amount of Ag adatoms can increase the possibility of intense interfacial intermixing between Ag and Pt atoms [32]. Once the interface is fully alloyed with the large amount of Ag, the initial Pt NP matrix can be destroyed and then the fully alloyed AgPt NPs can be formed. The fully alloyed NPs can gradually develop as large clusters as seen in the AFM scanning in Fig. S10. In the case of fully alloyed AgPt

NPs, no background Ag NPs were formed. The EDS phase maps in Fig. S12 further confirmed the alloyed phase according to the same elemental distribution of Pt Mα1 and Ag Lα1. In short, the dewetting process can be governed by the available Ag adatoms and activation energy in the system.

3.2. Optical properties of HyCoS AgPt NPs and FDTD simulation

Figure 3 shows the optical properties of HyCoS AgPt NPs fabricated with the deposition of 10 nm Ag coatings. In particular, the resonance peaks and dips at a specific wavelength and their intensity variation were observed along with the annealing. The extinction spectra are shown in Fig. 3(a). The 10-nm Ag thin film on bare sapphire showed a minor peak near the ultraviolet (UV) region at 390 nm and a broad peak region at 660 nm over the visible (VIS) region. The pure Pt NPs demonstrated peaks at 320 and 460 nm over the UV and VIS regions respectively, which can be correlated to the quadrupolar (QR) and dipolar resonance (DR) modes of NPs respectively [33]. The broader VIS peak of Ag film as compared to the pure Pt NPs can be due to the wide coverage of Ag thin film [28]. The AgPt HyCoS NPs at 0 °C showed the DR peak at ~ 465 nm, which is a slight red shift as compared to the pure Pt NP template as clearly seen in Fig. 3(a-2). Meanwhile, the extinction intensity was increased with the Ag coating, indicating an enhanced LSPR properties [34]. Interestingly, the extinction spectrum of 0 °C sample appeared to be the superposition of extinction spectra of Pt template and Ag film with the one weak peak in the UV and the other more intense peak in the VIS region. With the annealing at 400 °C, the resonance peak appeared at ~ 475 nm as the background Ag NPs were developing. Additionally, at 600 °C, the LSPR peak was further intensified, indicating the more intense resonance mode and narrower bandwidth [34]. The overall LSPR peak positions and shift are summarized in the magnified normalized extinction spectra in Fig. 3(a-1) and contour plots in Fig. 3(a-2). The color code of contour plot is given on the right side, representing the normalized intensity and the y-axis indicates the samples. The contour plot clearly visualizes the gradual bandwidth narrowing with slight red shift along with the increased annealing

temperature. The corresponding reflectance (R) and transmittance (T) are shown in Figs. 3(b) – 3(c), which matched well with the extinction results, exhibiting narrower dips at the UV region and broader dips at the VIS-NIR region. The dips in the reflectance spectra represent the absorption and scattering of photons, which appear as a peak in extinction spectra. The transmittance dips were developed due to the transmittance of the VIS-NIR portion of photons along with the annealing, which gives rise to the LSPR extinction peaks for the HyCoS AgPt NPs. The corresponding normalized R, T and contour plots were shown in Figs. 3(b-1) – 3(c-1) and Figs. 3(b-2) – 3(c-2), exhibiting the matching trends and gradual blue-shifts along with the narrower dips. The optical properties of AgPt NPs fabricated with 5 and 20 nm Ag coating can be found in Figs. S9 and S14. In the case of 5 nm Ag coating, generally the optical behavior was similar to the 10-nm coating set. The overall extinction intensity was lower as compared with 10-nm coating set indicating lower LSPR properties. The lower intensity maybe due to the lower Ag coating and decreased BG NP size by the lower Ag coating [34]. As for the AgPt NPs coated with 20 nm Ag, much broad extinction peaks were observed. Also, the extinction peaks were gradually red-shifted. The broadened peaks along with the increased SSD temperature might be due to the formation of much larger irregular NPs [31]. At 600 ºC, the extinction percentage was largely reduced, which can indicate lower LSPR properties [31,33].

The LSPR property analysis of various NP configurations was probed by the finite-difference time-domain (FDTD) simulation. The total field scattered field (TFSF) source was employed to analyze the scattering of plasmonic NPs, and the dimensions of NPs were adapted based on the AFM results. More details on the simulation parameters can be found in the supplementary section S-3. The schematics of Pt NPs and HyCoS AgPt NPs are shown in Figs. 3(d) – 3(e) and e-field distributions of top-views are shown in Figs. 3(d-1) – 3(e-1). The side-views are provided in Figs. S15(a-1) and S15(e-1). Other NP configurations are also simulated in Fig. S15. Generally, the e-field distributions were commonly observed at the edges of metallic NPs as the electromagnetic

field resonance occurs on the surface and edges of plasmonic structures [27]. Pure Pt NPs exhibited the maximum local e-field intensity (MLEI or E_{max}) of 5.21 and 5.30 in the simulation top- and side-views in Fig. 3(d-1) and S15(a-1). Then, the pure Ag NP of the same size showed the E_{max} of 6.81 and 7.02 in the top- and side-views in Figs. S15(b) and S15(b-1). The small background (BG) Ag NPs showed the E_{max} of 9.22 and 9.17 in the top- and side-views in Figs. S15(c) and S15(c-1) likely due to the increased NP density with more surface area. It was clearly seen that more hot spots are generated in the NP gaps based on the high density BG Ag NP coupling [27]. The fully alloyed NPs, i.e., with 20 nm Ag coating, demonstrated the E_{max} of 9.43 and 9.57 in the top- and side-views in Figs. S15(d) and S15(d-1). In addition, the AFM data incorporated FDTD simulation of fully alloyed NPs with 20 nm Ag coating showed a similar E_{max} of 10.54 in Fig. S14(d-1) based on the AFM image in Fig. S14(d). Finally, the HyCoS AgPt NPs demonstrated a largely improved resonance mode with the E_{max} of 18.2 and 17.8 in the top- and side-views in Figs. 3(e-1) and S15(e-1), which is nearly 3 times higher than the pure Pt and Ag NPs and nearly twice higher over the BG Ag and alloy NPs. In the hybrid core-shell (HyCoS) AgPt NP configuration, a thin Ag-shell is formed on the Pt core NP and thus a strong electromagnetic field resonance can occur on the AgPt core-shell surface. Also, the high-density BG Ag NPs can increase the surface coverage of NPs and hence the density of hot spots. The BG NPs are formed around the AgPt core-shell NPs and thus more interface can be created, resulting in more hot spots. With the AgPt core-shell NPs along with the high density BG NPs, significantly enhanced LSPR can result in the HyCoS NP configuration with the high maximum local e-field intensity [27]. As a result, the resonance intensity of HyCoS AgPt NPs was dramatically enhanced via the strong plasmonic coupling with abundant hot spots. The strong e-filed and numerous hot spots with the strong LSPR can significantly amplify the Raman signals of probe molecules and thus the HyCoS configuration is suitable for the plasmonic template for the SERS application.

3.3. 4-MBA SERS on AgPt HyCoS NPs

Figure 4 shows the SERS of 4-mercaptobenzoic acid (4-MBA) on the HyCoS AgPt NP substrates. According to the optical property and FDTD simulation analyses, the HyCoS AgPt with 10 nm Ag coating annealed at 600 °C was adapted as the plasmonic SERS template. To begin with, the c-plane bare sapphire showed a typical characteristic peak located at 750 cm^{-1} as seen in Fig. 4(a), which is assigned to the E_g vibrational mode [8]. The AgPt HyCoS NP showed no Raman spectra as metallic NPs do not exhibit Raman scattering. The E_g vibrational mode of sapphire was fully buried by the NPs. Subsequently, 20 µl 10^{-6} M 4-MBA was drop-casted on sapphire and no characteristic peaks of 4-MBA appeared since sapphire is not SERS active. The E_g mode of sapphire showed reduced peak intensity with the 4-MBA deposition. To probe the SERS activity of prepared templates, the 4-MBA molecule was applied on HyCoS AgPt NPs. Then, it exhibited a series of intense characteristic peaks of 4-MBA. The intensity was reduced by 4 times to fit in. Here, the characteristic peaks of 4-MBA at 1075 cm^{-1} can be attributed to C-H deforming vibration and the band at about 1585 cm^{-1} arise from the aromatic ring (C = C) breathing mode [35,36]. The band at 688 cm^{-1} can be related to a mixture of OCO bending and the COO^- stretching mode is found at 1375 cm^{-1} [36]. The band at 1181 belongs to the C–S stretching mode [37]. This long-range SERS enhancement on the HyCoS AgPt NPs can be related to the electromagnetic mechanism (EM) enhancement, which will be discussed in the later section [8,38]. Subsequently, the 2:1 mixture solution of 4-MBA and GQD was drop-casted on the HyCoS substrate. Surprisingly, much-enhanced signal was obtained, which was about 10 times higher than that obtained without the GQD mixture. The signal intensity was reduced by 20 times to fit in. The bar graph summarized the intensity change in the characteristic peaks of 4-MBA at 1075, 1181, 1375 and 1585 cm^{-1} in Fig. 4(a-1). The summary clearly showed that all the characteristic peaks of 4-MBA were sharply increased with the addition of GQDs. Especially, the peaks at 800, 1375 cm^{-1} and other small peaks showed much-improved signal intensity, which was weak when the GQD was not mixed. The inset shows the 4-MBA skeletal molecule, which has the

thiol (SH) and carboxylic (COOH) group and benzene π-electron system as binding sites. The Raman response depends upon the binding of 4-MBA molecules with the substrate and the intensity depends on the number of molecules adsorbed [39]. In the case of HyCoS + GQD substrate, the applied amount of 4-MBA was indeed reduced while the signal intensity was increased. For example, 20 µl 10^{-6} M 4-MBA was applied on the HyCoS NPs and 13 µl 10^{-6} M 4-MBA and 7 µl of GQD applied on HyCoS + GQD substrate. The spectral enhancement of 4-MBA can be attributed to the synergetic effect of HyCoS NPs and GQDs, combining the electromagnetic mechanism (EM) and chemical enhancement mechanism (CM) [8].

To further study the SERS of 4-MBA on the HyCoS AgPt NPs, various molarities of 4-MBA were employed as seen in Fig. 4(b). Gradually intensified SERS peaks were clearly observed along with the molarity variation from 10^{-8} to 10^{-3} M in Fig. 4(b). The SERS peak intensity is summarized in Fig. 4(b-1) along with the molarity variation and gradually intensified SERS trend can be clearly seen from the bar graph as well. This can indicate the superior effectiveness of plasmonic AgPt HyCoS NPs for the SERS template without the saturation of peak intensity along with the molarity variation. For SERS performance comparison, the 10:1 mixture (10^{-6} M 4-MBA + GQD) was applied on a bare Ag NP substrate in Fig. S18, and the HyCoS AgPt NPs demonstrated around 3 times higher SERS intensity over that bare Ag NPs. Generally, the Ag NPs are known for a good SERS substate due to their inherently strong plasmonic properties. The HyCoS AgPt NPs can demonstrate superior SERS platform due to its unique design, i.e., AgPt core-shell and high-density BG Ag NPs in a single platform. A strong electromagnetic field resonance can occur on the AgPt core-shell surface and numerous hot spots can be generated by the high-density BG Ag NPs as seen in the simulation discussion. The combination of AgPt core-shell and high-density BG Ag NPs in a single platform can give a rise to the strong EM effect and the SERS signal can be largely improved.

Additional investigation on the mixing approach was conducted by varying the mixing ratio of 4-MBA and GQD as seen in Fig. 4(c). From the 10^{-6} M 4-MBA, the SERS signals were sharply

increased with the 1:1, 2:1 and 10:1 ratio as summarized in Fig. 4(c-1). Specific values of SERS intensities are summarized in Tables S1 – S2. Here, the lower concentration of GQDs, i.e., 10:1 (4-MBA : GQD) mixture as compared with the 1:1 and 2:1 mixture, exhibited a stronger SERS enhancement. This can indicate that a sufficient amount of 4-MBA molecules is necessary for an appropriate charge transfer from the GQDs to the 4-MBA molecules through the $\pi - \pi$ interaction by the chemical mechanism (CM) [8,29]. In other words, excessive amount of GQDs, i.e., 1:1 and 2:1 mixtures, may lead to the less SERS enhancement of 4-MBA or blockage of EM enhancement [29]. As mentioned, the 4-MBA has the thiol (SH) and carboxylic (COOH) group and benzene π-electron system as binding sites and the SERS enhancement can depend on the binding of 4-MBA molecules on GQDs and also on the number of molecules adsorbed [39].

The Raman signal of GQDs was measured on sapphire in Fig. S16 and it showed a typical amorphous D band and graphitic G band at 1375 and 1585 cm^{-1} [40]. Here, coincidently, the graphitic G band is at the same position of 1585 cm^{-1} Raman band of 4-MBA. Initially, the SERS enhancement of 4-MBA by the mixing approach appeared to be the superposition of GQD and 4-MBA Raman bands at a quick look. But then it was found that it is not a superposition as other peaks were also clearly enhanced with the addition of GQDs. Indeed, the 1375 and 1585 cm^{-1} D & G bands did not appear with BT in the next experiment. In short, the HyCoS AgPt NPs demonstrated an excellent SERS substate with the strong EM enhancement and the mixing approach with the GQD demonstrated a further increased SERS signal through the combination of EM and CM enhancement. The GQD has numerous accessible edges where the target molecules can be adsorbed and sufficient charge transfer can occur and appropriate amount of GQD addition is necessary [41].

3.4. BT SERS on AgPt HyCoS NPs

Figure 5 shows the SERS of benzenethiol (BT) on the plasmonic AgPt HyCoS NP template. The BT concentration was varied from 10^{-3} to 10^{-7} M as seen in Fig. 5(a) and the SERS intensity of four

characteristic BT peaks at various concentrations is summarized in Fig. 5(a-1) and Table S3. The SERS spectra of BT were clearly observable at 999, 1020, 1069, and 1572 cm^{-1} for all concentrations and the SERS intensity was gradually increased with the increased molar concentration. The band at 999 cm^{-1} can be indexed to the in-plain ring-breathing mode and the 1020 cm^{-1} can be related to the in-plain C–H bending mode [42]. The peak at 1069 cm^{-1} can correspond to the in-plane ring breathing mode coupled with the C–S stretching mode while the peak at 1572 cm^{-1} can be related to the C–C stretching mode [42,43] The SERS signal was again gradually increased along with the increased molar concentration, which can be due to the numerous hot spots and strong LSPS in the vicinity of metallic NPs [44]. The HyCoS AgPt NPs demonstrated an excellent SERS substate for the BT as well. The BT molecule has a benzene ring with a thiol (SH) as binding site [45] and it is not very often used due to too the exceptional smell. The SERS effect was further analyzed for three different mixtures of 10^{-5} M BT and GQDs as seen in Fig. 5(b). The SERS intensity at different mixture ratio is plotted for various characteristic BT peaks in Fig. 5(b-1). As compared with the initial BT SERS intensity, significantly enhanced SERS intensities were also clearly observed for all BT and GQD mixtures. Similar to the 4-MBA, the 10:1 mixture ratio demonstrated the highest SERS intensity and 1:1 mixture showed the lowest intensity, indicating that an appropriate amount of GQD is beneficial for sufficient SERS enhancement as discussed. Now, the 1375 and 1585 cm^{-1} D & G bands of GQD did not appear for BT SERS. The GQDs can transfer the charges to the highest occupied molecular orbital (HOMO) and lowest unoccupied molecular orbital (LUMO) levels of BT through the numerous accessible edges with the laser excitation by the CM [23]. The direct contact between BT and GQDs with appropriate amount of GQD can facilitate the charge transfer process via the $\pi - \pi$ interaction, further enhancing the SERS response [23,46]. The optimal condition was found to be 10:1 (BT : GQD) and an appropriate amount of GQD can ensure the strong interaction and sufficient charge transfer from GQD to HOMO and LUMO levels of BT [46].

3.5. SERS enhancement factor, uniformity, and enhancement mechanism

Figure 6 shows the summarized comparison of SERS intensity of 4-MBA and BT mixed with GQDs on the AgPt HyCoS NP template and the enhancement mechanism. In Figs. 6(a) – 6(b), the mixture approach demonstrated significant enhancement of SERS signals of both 4-MBA and BT on the HyCoS AgPt NPs and the optimal mixture ratio for both 4-MBA and BT and GQD was found to be 10:1. While the GQDs can provide charge transfer to the probe molecules, an excessive amount can result in lower enhancements or sufficient amount of probe molecules is still necessary for the optimum SERS performance. Figure 6(c) shows the bar graph of SERS comparison and around 10 times of SERS enhancements were observed for both 4-MBA and BT from the SERS enhancement on the AgPt HyCoS NPs. In addition, the SERS enhancement factor (EF) of the hybrid platform for 4-MBA and BT was calculated for quantitative analysis of SERS efficiency base on the following formula [11,47]: $EF = \frac{I_{SERS} N_{solid}}{I_{solid} N_{SERS}}$, where the I_{SERS} and I_{solid} are the SERS intensities of the probe molecules and Raman intensities on bare substrate. N_{solid} and N_{SERS} present the numbers of probe molecules in the laser spot. The bare Raman spectra of 10^{-6} M 4-MBA and 10^{-5} M BT on sapphire can be found in Fig. S17 and more details on the EF calculation can be found in the supplementary section S-4. The EF was calculated to be ~ 10^6 for the 10^{-6} M 4-MBA on the plasmonic HyCoS AgPt NP template. Then, the EF was further enhanced to ~10^7 for the 10:1 mixture with the addition of GQD. For 10^{-5} M BT, the EF was found to be ~10^4 via the EM enhancement and can reach ~ 10^5 via the mixing approach. Specific values of enhancement factor for 4-MBA and BT at different peak positions are provided in Tables. S5 – S6.

To probe the uniformity and reproducibility of hybrid SERS platform, a series of SERS analyses was performed on the HyCoS AgPt NPs at different positions as seen in Fig. S19. The 10:1 mixture (10^{-6} M 4-MBA + GQD) was applied on 3 samples of AgPt HyCoS NPs and each sample was tested for 9 locations as seen in Fig. S19(a). Similar intensity of SERS spectra were obtained at 9 locations of 3 AgPt HyCoS NP samples and the characteristic peaks of 4-MBA were clearly

observed as seen in Figs. S19(b) – S19(d). The HyCoS AgPt NP demonstrated excellent reproducibility with the 3 samples and all 3 samples demonstrated similar spectral shapes and intensities of 4-MBA. The uniform spectral shape and intensity can indicate that the HyCoS AgPt NP template can offer stable SERS measurements throughout the substrate. The SERS intensities at 1585 cm^{-1} for the sample 1 were plotted for relative standard deviation (RSD) calculation for more quantitative analysis in Fig. S20. More details on the RSD calculation can be found in the supplementary section S-5. The RSD of sample 1 at 1585 cm^{-1} was calculated to be 6.65%, which indicates that the HyCoS AgPt NPs demonstrated an excellent uniformity of hybrid SERS approach. Generally, the solid-state diffusion-based NPs can offer a uniform SERS substrate as the NPs are quite uniform. The NPs are formed through thermal diffusion at high temperature and the metallic elements strongly adhere to the substate. In the hybrid SERS approach, a well-dispersed mixture of probe molecules and GQDs is also important. For this, the mixture solution was vigorously shaken and then ultrasonicated for 10 min. During the ultrasonication, uniform $\pi - \pi$ interaction can be established between the probe molecules and GQDs. In conclusion, the hybrid SERS approach of GQD and 4-MBA mixture can demonstrate superior reproducibility and uniformity on the HyCoS AgPt NPs.

In terms of enhancement mechanism, firstly, the electromagnetic field distribution of hybrid SERS platform was evaluated by the FDTD simulation with the addition of GQDs on the AgPt HyCoS NPs as seen in Fig. 6(d). The GQDs were placed on the top of metallic NPs for the consistency with the experimental set-up as illustrated in the schematic in Fig. 6(d-1). Strongly localized e-field can be clearly observed between the gaps of metallic NPs with the enhanced MLEI values of 26.8 and 25.4 as seen by the top- and side-views of FDTD simulation in Figs. 6(d-2) – 6(d-3). The FDTD simulation demonstrated a higher e-field intensity of hybrid SERS platform over the HyCoS AgPt NPs, which is almost 5 times higher than the pure metallic Pt NPs. The excellent SERS performances can be attributed to the electromagnetic mechanism (EM) by the HyCoS AgPt NPs and

chemical mechanism (CM) by the GQDs. The schematic of EM and CM contributions are illustrated in Fig. 6(e). In terms of EM enhancement, the HyCoS AgPt NPs demonstrated a superior SERS platform due to the unique combination of AgPt core-shell and high-density background (BG) Ag NPs. The AgPt core-shell NP can demonstrate a strong electromagnetic field resonance on the surface and the high-density BG Ag NPs can exhibit abundant hot spot density over the substrate [13,48]. The BG Ag NPs can also demonstrate the electromagnetic coupling between NPs and thus the overall LSPR can be significantly improved. The combination of AgPt core-shell and high-density BG Ag NPs in a single substrate can give a rise to the strong LSPR and the SERS signal of probe molecules can be largely improved by the EM effect [13,48] as illustrated in Fig. 6(e). At the same time, the CM enhancement can be described by the charge transfer process from the GQD to the probe molecules. Initially, relatively weak resonant Raman scattering can occur in the energy gap between the highest occupied molecular orbital (HOMO) and lowest unoccupied molecular orbital (LUMO) of probe molecules [49]. With the mixed hybrid SERS substrate, abundant charges can be transferred to the HOMO and LUMO of probe molecules from the GQDs as illustrated in Fig. 6(e) [23]. The GQDs possess high adsorption capacity for the molecules with its large surface area and efficient charge transfer characteristics by the unique π-conjugate. Thus the Raman signals can be significantly enhanced via the $\pi - \pi$ interaction and charge transfer [8,19,50]. In the hybrid SERS configuration, the hot carriers by the numerous spots and enhanced LSPR from the HyCoS AgPt NPs can be combined with the charge transfer from the GQDs to the probe molecules and thus the SERS signals can be significantly amplified through the combination of electromagnetic mechanism (EM) and chemical mechanism (CM) as illustrated in Fig. 6(e) [23][51].

4. Conclusion

In summary, hybrid core-shell (HyCoS) AgPt NPs were successfully fabricated via a two-step solid-state dewetting (SSD) process and the LSPR and optical properties along with the morphology

evolution was thoroughly investigated as a function of Ag coating thickness and annealing temperature. The FDTD simulation was further conducted to probe the electromagnetic field distribution and resonance intensity. The AgPt HyCoS NPs with 10 nm Ag coating annealed at 600 ºC demonstrated the best LSPR characteristics with the highest maximum local e-field intensity and thus was selected as a plasmonic template along with GQDs for the hybrid SERS application of 4-MBA and BT. The proposed hybrid SERS approach, i.e., mixing application of probe molecules and GQD on AgPt HyCoS NPs, indicated several orders of enhancement for both 4-MBA and BT. The mixture ratio of 10:1 of probe molecules : GQD was found to exhibit the highest improvement and the enhancement factor (EF) can reach ~10^7 for 10^{-6} M 4-MBA and ~10^5 for 10^{-5} M BT. The mixture application of GQD and probe molecules can demonstrate superior uniformity and reproducibility and on the HyCoS AgPt NPs due to the excellent uniform nature of SSD-based NPs and high absorption capacity of GQDs. RSD value of 6.65% was obtained from the 9 positions in a sample. The hybrid SERS approach with the combination of GQD and HyCoS AgPt NPs by utilizing both CM and EM can find a significant potential for the SERS platform.

CRediT authorship contribution statement

Shusen Lin: Methodology, Investigation, Validation, Writing – original draft, review & editing. **Md Ahasan Habib:** Investigation, Data acquisition. **Shalmali Burse:** Investigation, Data acquisition. **Rutuja Mandavkar:** Investigation, Data acquisition. **Mehedi Hasan Joni:** Investigation, Data acquisition. **Sundar Kunwar**: Methodology, Investigation, Validation and Funding acquisition. **Jihoon Lee:** Conceptualization, project management, Funding acquisition, Writing – review & editing.

Declaration of Competing Interest

The authors declare that they have no known competing financial interests or personal relationships that could have appeared to influence the work reported in this paper.

Data Availability

Data are available upon request to corresponding authors.

Acknowledgments

Financial supports by the National Research Foundation of Korea (NRF) grant funded by the Korea government (MSIT) (Nos. NRF-2022R1H1A2091290 and NRF-2018R1A6A1A03025242) is gratefully acknowledged. The work was conducted during the sabbatical of Kwangwoon University in 2022. The work at Los Alamos National Laboratory was supported by the NNSA's Laboratory Directed Research and Development Program, and was performed, in part, at the CINT, an Office of Science User Facility operated for the U.S. Department of Energy Office of Science. Los Alamos National Laboratory, an affirmative action equal opportunity employer, is managed by Triad National Security, LLC for the U.S. Department of Energy's NNSA, under contract 89233218CNA000001. Special appreciations to Ms. So Hee Kim from the Korea Institute of Science

and Technology (KIST) for the SEM-EDX characterizations.

References:

[1] O. Guselnikova, H. Lim, H.-J. Kim, S.H. Kim, A. Gorbunova, M. Eguchi, P. Postnikov, T. Nakanishi, T. Asahi, J. Na, Y. Yamauchi, New Trends in Nanoarchitectured SERS Substrates: Nanospaces, 2D Materials, and Organic Heterostructures, Small. 18 (2022) 2107182. https://doi.org/https://doi.org/10.1002/smll.202107182.

[2] I. Deneme, G. Liman, A. Can, G. Demirel, H. Usta, Enabling three-dimensional porous architectures via carbonyl functionalization and molecular-specific organic-SERS platforms, Nat. Commun. 12 (2021) 6119. https://doi.org/10.1038/s41467-021-26385-7.

[3] Y. Peng, C. Lin, L. Long, T. Masaki, M. Tang, L. Yang, J. Liu, Z. Huang, Z. Li, X. Luo, J.R. Lombardi, Y. Yang, Charge-Transfer Resonance and Electromagnetic Enhancement Synergistically Enabling MXenes with Excellent SERS Sensitivity for SARS-CoV-2 S Protein Detection, Nano-Micro Lett. 13 (2021) 52. https://doi.org/10.1007/s40820-020-00565-4.

[4] J. Liu, Q. Ma, Z. Huang, G. Liu, H. Zhang, Recent Progress in Graphene-Based Noble-Metal Nanocomposites for Electrocatalytic Applications, Adv. Mater. 31 (2019) 1800696. https://doi.org/10.1002/adma.201800696.

[5] S.-J. Choi, H. Yu, J.-S. Jang, M.-H. Kim, S.-J. Kim, H.S. Jeong, I.-D. Kim, Nitrogen-Doped Single Graphene Fiber with Platinum Water Dissociation Catalyst for Wearable Humidity Sensor, Small. 14 (2018) 1703934. https://doi.org/10.1002/smll.201703934.

[6] Samriti, V. Rajput, R.K. Gupta, J. Prakash, Engineering metal oxide semiconductor nanostructures for enhanced charge transfer: fundamentals and emerging SERS applications, J. Mater. Chem. C. 10 (2022) 73–95. https://doi.org/10.1039/D1TC04886D.

[7] R.D. Norton, H.T. Phan, S.N. Gibbons, A.J. Haes, Quantitative Surface-Enhanced Spectroscopy, Annu. Rev. Phys. Chem. 73 (2022) 141–162. https://doi.org/10.1146/annurev-physchem-082720-033751.

[8] R. Mandavkar, S. Lin, S. Pandit, R. Kulkarni, S. Burse, M.A. Habib, S. Kunwar, J. Lee, Hybrid SERS platform by adapting both chemical mechanism and electromagnetic mechanism enhancements: SERS of 4-ATP and CV by the mixture with GQDs on hybrid PdAg NPs, Surfaces and Interfaces. 33 (2022) 102175. https://doi.org/https://doi.org/10.1016/j.surfin.2022.102175.

[9] R. Mandavkar, S. Lin, R. Kulkarni, S. Burse, M.A. Habib, S. Kunwar, J. Lee, Dual-step photocarrier injection by mixture layer of ZnO QDs and MoS2 NPs on hybrid PdAu NPs, Mater. Res. Bull. 151 (2022) 111832. https://doi.org/https://doi.org/10.1016/j.materresbull.2022.111832.

[10] S. Kunwar, S. Pandit, R. Kulkarni, R. Mandavkar, S. Lin, M.Y. Li, J. Lee, Hybrid device architecture using plasmonic nanoparticles, graphene quantum dots, and titanium dioxide for UV photodetectors, ACS Appl. Mater. Interfaces. 13 (2021) 3408–3418. https://doi.org/10.1021/acsami.0c19058.

[11] T. Wu, H. Zheng, Y. Kou, X. Su, N.R. Kadasala, M. Gao, L. Chen, D. Han, Y. Liu, J. Yang, Self-sustainable and recyclable ternary Au@Cu2O–Ag nanocomposites: application in ultrasensitive SERS detection and highly efficient photocatalysis of organic dyes under visible light, Microsystems Nanoeng. 7 (2021). https://doi.org/10.1038/s41378-021-00250-5.

[12] B.K. Sahu, A. Dwivedi, K.K. Pal, R. Pandian, S. Dhara, A. Das, Optimized Au NRs for efficient SERS and SERRS performances with molecular and longitudinal surface plasmon resonance, Appl. Surf. Sci. 537 (2021) 147615. https://doi.org/https://doi.org/10.1016/j.apsusc.2020.147615.

[13] G. Kaur, S. Tanwar, V. Kaur, R. Biswas, S. Saini, K.K. Haldar, T. Sen, Interfacial design of gold/silver core–shell nanostars for plasmon-enhanced photocatalytic coupling of 4-aminothiophenol, J. Mater. Chem. C. 9 (2021) 15284–15294. https://doi.org/10.1039/D1TC03733A.

[14] O. Nasr, Y.-Y. Lin, Y.-S. Chou, C.-W. Huang, W.-S. Chuang, S.-W. Lee, C.-Y. Chen, Surface-enhanced Raman scattering of CoTiO3@Ag nanofibers for high-performance sensing applications, Appl. Surf. Sci. 573 (2022) 151509. https://doi.org/https://doi.org/10.1016/j.apsusc.2021.151509.

[15] B. Sharma, R.R. Frontiera, A.-I. Henry, E. Ringe, R.P. Van Duyne, SERS: Materials, applications, and the future, Mater. Today. 15 (2012) 16–25. https://doi.org/https://doi.org/10.1016/S1369-7021(12)70017-2.

[16] S. Lee, I. Jung, J. Son, S. Lee, M. Park, J.-E. Kim, W. Park, J. Lee, J.-M. Nam, S. Park, Heterogeneous Component Au (Outer)–Pt (Middle)–Au (Inner) Nanorings: Synthesis and Vibrational Characterization on Middle Pt Nanorings with Surface-Enhanced Raman Scattering, ACS Nano. 16 (2022) 11259–11267. https://doi.org/10.1021/acsnano.2c04633.

[17] H.T. Phan, A.J. Haes, Impacts of pH and Intermolecular Interactions on Surface-Enhanced Raman Scattering Chemical Enhancements, J. Phys. Chem. C. 122 (2018) 14846–14856. https://doi.org/10.1021/acs.jpcc.8b04019.

[18] G.M. Das, S. Managò, M. Mangini, A.C. De Luca, Biosensing Using SERS Active Gold Nanostructures, Nanomaterials. 11 (2021). https://doi.org/10.3390/nano11102679.

[19] S.M. Mousavi, S.A. Hashemi, M. Yari Kalashgrani, D. Kurniawan, A. Gholami, V. Rahmanian, N. Omidifar, W.-H. Chiang, Recent Advances in Inflammatory Diagnosis with

Graphene Quantum Dots Enhanced SERS Detection, Biosensors. 12 (2022). https://doi.org/10.3390/bios12070461.

[20] X. Liang, N. Li, R. Zhang, P. Yin, C. Zhang, N. Yang, K. Liang, B. Kong, Carbon-based SERS biosensor: from substrate design to sensing and bioapplication, NPG Asia Mater. 13 (2021) 8. https://doi.org/10.1038/s41427-020-00278-5.

[21] D. Liu, X. Chen, Y. Hu, T. Sun, Z. Song, Y. Zheng, Y. Cao, Z. Cai, M. Cao, L. Peng, Y. Huang, L. Du, W. Yang, G. Chen, D. Wei, A.T.S. Wee, D. Wei, Raman enhancement on ultra-clean graphene quantum dots produced by quasi-equilibrium plasma-enhanced chemical vapor deposition, Nat. Commun. 9 (2018) 1–10. https://doi.org/10.1038/s41467-017-02627-5.

[22] F. Zou, H. Zhou, T. Van Tan, J. Kim, K. Koh, J. Lee, Dual-Mode SERS-Fluorescence Immunoassay Using Graphene Quantum Dot Labeling on One-Dimensional Aligned Magnetoplasmonic Nanoparticles, ACS Appl. Mater. Interfaces. 7 (2015) 12168–12175. https://doi.org/10.1021/acsami.5b02523.

[23] J. Jin, W. Song, J. Wang, L. Li, Y. Tian, S. Zhu, Y. Zhang, S. Xu, B. Yang, B. Zhao, A highly sensitive SERS platform based on small-sized Ag/GQDs nanozyme for intracellular analysis, Chem. Eng. J. 430 (2022) 132687. https://doi.org/https://doi.org/10.1016/j.cej.2021.132687.

[24] S. Kunwar, S. Pandit, J.H. Jeong, J. Lee, Improved Photoresponse of UV Photodetectors by the Incorporation of Plasmonic Nanoparticles on GaN Through the Resonant Coupling of Localized Surface Plasmon Resonance, Nano-Micro Lett. 12 (2020) 1–16. https://doi.org/10.1007/s40820-020-00437-x.

[25] S. Yang, F. Xu, S. Ostendorp, G. Wilde, H. Zhao, Y. Lei, Template-Confined Dewetting Process to Surface Nanopatterns: Fabrication, Structural Tunability, and Structure-Related Properties, Adv. Funct. Mater. 21 (2011) 2446–2455. https://doi.org/10.1002/adfm.201002387.

[26] F. Leroy, Borowik, F. Cheynis, Y. Almadori, S. Curiotto, M. Trautmann, J.C. Barbé, P. Müller, How to control solid state dewetting: A short review, Surf. Sci. Rep. 71 (2016) 391–409. https://doi.org/10.1016/j.surfrep.2016.03.002.

[27] S. Lin, R. Mandavkar, M.A. Habib, S. Burse, T. Khalid, M.H. Joni, M.-Y. Li, S. Kunwar, J. Lee, Investigation on the AgPt and AgPd hybrid alloy nanoparticles (HANPs) for the hybrid MoS2/ZnO/HANP UV photodetector application, Appl. Surf. Sci. 611 (2023) 155559. https://doi.org/https://doi.org/10.1016/j.apsusc.2022.155559.

[28] S. Pandit, S. Kunwar, R. Kulkarni, R. Mandavka, S. Lin, J. Lee, Fabrication of hybrid Pd@Ag core-shell and fully alloyed bi-metallic AgPd NPs and SERS enhancement of Rhodamine 6G by a unique mixture approach with graphene quantum dots, Appl. Surf. Sci. 548 (2021) 149252. https://doi.org/10.1016/j.apsusc.2021.149252.

[29] R. Mandavkar, S. Lin, R. Kulkarni, S. Pandit, S. Burse, M.A. Habib, P. Pandey, S. Kunwar, J. Lee, Dual-step hybrid SERS scheme through the blending of CV and MoS2 NPs on the AuPt core-shell hybrid NPs, J. Mater. Sci. Technol. 107 (2022) 1–13. https://doi.org/https://doi.org/10.1016/j.jmst.2021.08.022.

[30] M.A. Asoro, D. Kovar, P.J. Ferreira, In situ Transmission Electron Microscopy Observations of Sublimation in Silver Nanoparticles, ACS Nano. 7 (2013) 7844–7852. https://doi.org/10.1021/nn402771j.

[31] M. Sui, S. Kunwar, P. Pandey, J. Lee, Strongly confined localized surface plasmon resonance (LSPR) bands of Pt, AgPt, AgAuPt nanoparticles, Sci. Rep. 9 (2019) 1–14. https://doi.org/10.1038/s41598-019-53292-1.

[32] Y. Ding, F. Fan, Z. Tian, Z.L. Wang, Atomic Structure of Au−Pd Bimetallic Alloyed Nanoparticles, J. Am. Chem. Soc. 132 (2010) 12480–12486. https://doi.org/10.1021/ja105614q.

[33] R. Mandavkar, R. Kulkarni, S. Lin, S. Pandit, S. Burse, M. Ahasan Habib, P. Pandey, S. Hee Kim, M.-Y. Li, S. Kunwar, J. Lee, Significantly improved photo carrier injection by the MoS2/ZnO/HNP hybrid UV photodetector architecture, Appl. Surf. Sci. 574 (2022) 151739. https://doi.org/https://doi.org/10.1016/j.apsusc.2021.151739.

[34] L. Yan, Y. Yan, L. Xu, R. Ma, F. Jiang, X. Xu, Large range localized surface plasmon resonance of Ag nanoparticles films dependent of surface morphology, Appl. Surf. Sci. 367 (2016) 563–568. https://doi.org/https://doi.org/10.1016/j.apsusc.2016.01.238.

[35] F. Wang, R.G. Widejko, Z. Yang, K.T. Nguyen, H. Chen, L.P. Fernando, K.A. Christensen, J.N. Anker, Surface-Enhanced Raman Scattering Detection of pH with Silica-Encapsulated 4-Mercaptobenzoic Acid-Functionalized Silver Nanoparticles, Anal. Chem. 84 (2012) 8013–8019. https://doi.org/10.1021/ac3018179.

[36] Z. Yu, L. Chen, Y. Park, Q. Cong, X. Han, B. Zhao, Y.M. Jung, The mechanism of an enzymatic reaction-induced SERS transformation for the study of enzyme–molecule interfacial interactions, Phys. Chem. Chem. Phys. 18 (2016) 31787–31795. https://doi.org/10.1039/C6CP05978C.

[37] S. Liu, X. Tian, J. Guo, X. Kong, L. Xu, Q. Yu, A.X. Wang, Multi-functional plasmonic fabrics: A flexible SERS substrate and anti-counterfeiting security labels with tunable encoding information, Appl. Surf. Sci. 567 (2021) 150861. https://doi.org/https://doi.org/10.1016/j.apsusc.2021.150861.

[38] C.K.A. Nyamekye, S.C. Weibel, E.A. Smith, Directional Raman scattering spectra of metal–sulfur bonds at smooth gold and silver substrates, J. Raman Spectrosc. 52 (2021) 1246–1255.

https://doi.org/https://doi.org/10.1002/jrs.6124.

[39] S. Zhu, C. Fan, J. Wang, J. He, E. Liang, M. Chao, Realization of high sensitive SERS substrates with one-pot fabrication of Ag–Fe3O4 nanocomposites, J. Colloid Interface Sci. 438 (2015) 116–121. https://doi.org/https://doi.org/10.1016/j.jcis.2014.09.015.

[40] V.A. Chhabra, R. Kaur, N. Kumar, A. Deep, C. Rajesh, K.-H. Kim, Synthesis and spectroscopic studies of functionalized graphene quantum dots with diverse fluorescence characteristics, RSC Adv. 8 (2018) 11446–11454. https://doi.org/10.1039/C8RA01148F.

[41] Y. Liu, H. Ma, X.X. Han, B. Zhao, Metal–semiconductor heterostructures for surface-enhanced Raman scattering: synergistic contribution of plasmons and charge transfer, Mater. Horizons. 8 (2021) 370–382. https://doi.org/10.1039/D0MH01356K.

[42] Y. Lee, J. Lee, T.K. Lee, J. Park, M. Ha, S.K. Kwak, H. Ko, Particle-on-Film Gap Plasmons on Antireflective ZnO Nanocone Arrays for Molecular-Level Surface-Enhanced Raman Scattering Sensors, ACS Appl. Mater. Interfaces. 7 (2015) 26421–26429. https://doi.org/10.1021/acsami.5b09947.

[43] G. Barbillon, A. Ivanov, K.A. Sarychev, Hybrid Au/Si Disk-Shaped Nanoresonators on Gold Film for Amplified SERS Chemical Sensing, Nanomater. . 9 (2019). https://doi.org/10.3390/nano9111588.

[44] R. Pilot, R. Signorini, C. Durante, L. Orian, M. Bhamidipati, L. Fabris, A Review on Surface-Enhanced Raman Scattering, Biosensors. 9 (2019). https://doi.org/10.3390/bios9020057.

[45] F. Sun, D.D. Galvan, P. Jain, Q. Yu, Multi-functional, thiophenol-based surface chemistry for surface-enhanced Raman spectroscopy, Chem. Commun. 53 (2017) 4550–4561. https://doi.org/10.1039/C7CC01577A.

[46] V. Sharma, N.N. Som, S.B. Pillai, P.K. Jha, Utilization of doped GQDs for ultrasensitive detection of catastrophic melamine: a new SERS platform, Spectrochim. Acta Part A Mol. Biomol. Spectrosc. 224 (2020) 117352.

[47] P.A. Mercadal, E.R. Encina, J.E.L. Villa, E.A. Coronado, A New Figure of Merit to Assess the SERS Enhancement Factor of Colloidal Gold Nanoparticle Aggregates, J. Phys. Chem. C. 125 (2021) 4056–4065. https://doi.org/10.1021/acs.jpcc.0c09122.

[48] B. Tim, P. Błaszkiewicz, M. Kotkowiak, Recent Advances in Metallic Nanoparticle Assemblies for Surface-Enhanced Spectroscopy, Int. J. Mol. Sci. 23 (2022). https://doi.org/10.3390/ijms23010291.

[49] E. Ashok Kumar, T.- Jiann Wang, Y.-H. Chang, Ultrasensitive SERS substrates based on Au nanoparticles photo-decorated on Cu2O microspheres for the detection of rhodamine B and methylene blue, Appl. Surf. Sci. 585 (2022) 152696.

https://doi.org/https://doi.org/10.1016/j.apsusc.2022.152696.

[50] A. Alsalme, T. Pooventhiran, N. Al-Zaqri, D.J. Rao, R. Thomas, Structural, physico-chemical landscapes, ground state and excited state properties in different solvent atmosphere of Avapritinib and its ultrasensitive detection using SERS/GERS on self-assembly formation with graphene quantum dots, J. Mol. Liq. 322 (2021) 114555. https://doi.org/https://doi.org/10.1016/j.molliq.2020.114555.

[51] J.-F. Li, Y.-J. Zhang, S.-Y. Ding, R. Panneerselvam, Z.-Q. Tian, Core–Shell Nanoparticle-Enhanced Raman Spectroscopy, Chem. Rev. 117 (2017) 5002–5069. https://doi.org/10.1021/acs.chemrev.6b00596.

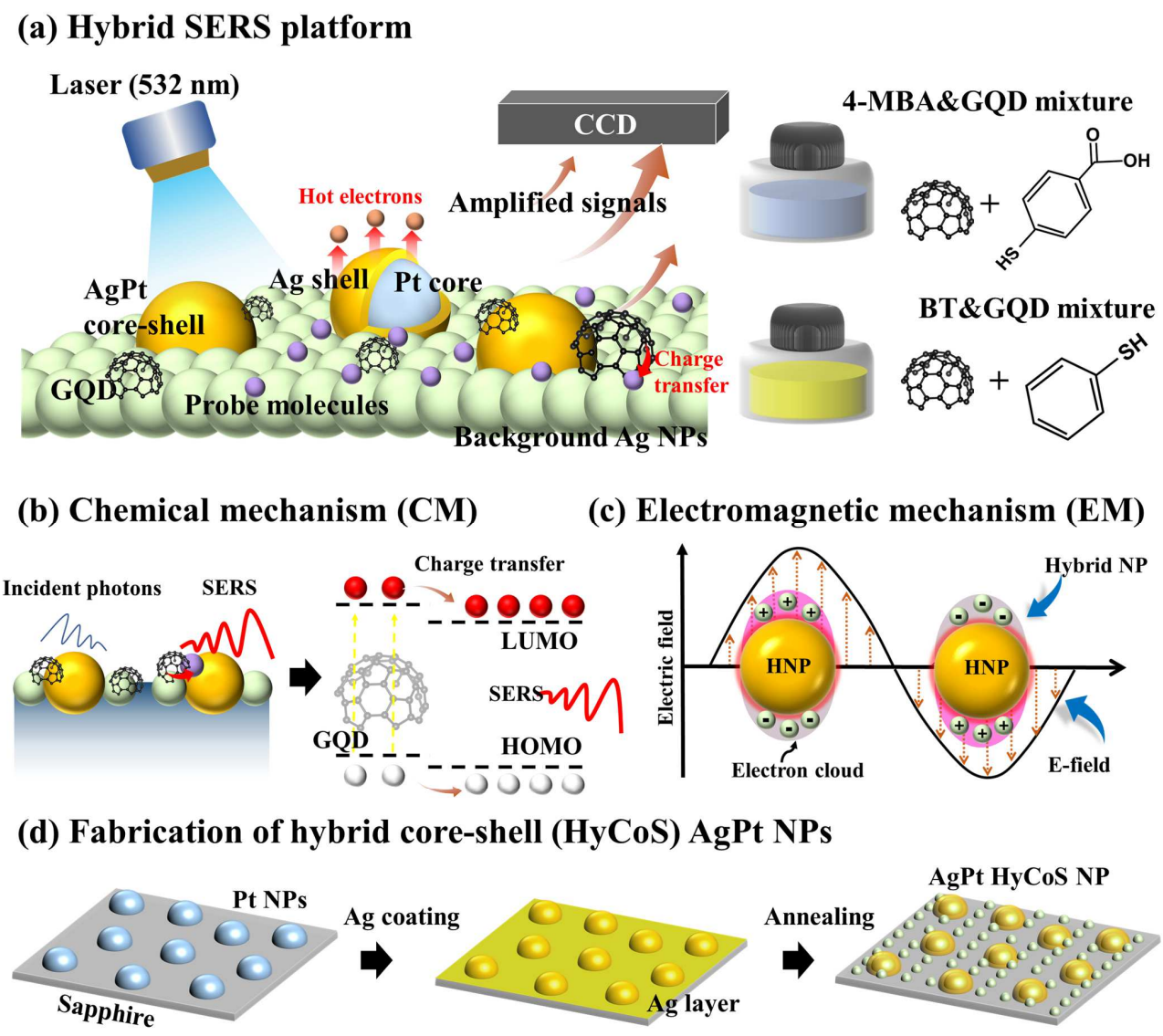

Figure 1: (a) Schematic of hybrid surface-enhanced Raman spectroscopy (SERS) platform for 4-mercaptobenzoic acid (4-MBA) and benzenethiol (BT). (b) Schematic of chemical mechanism (CM) and charge transfer process. (c) Schematic of localized surface plasmon resonance (LSPR). (d) Fabrication steps of hybrid core-shell (HyCoS) AgPt nanoparticles (NPs) via dual-step solid state dewetting (SSD) process.

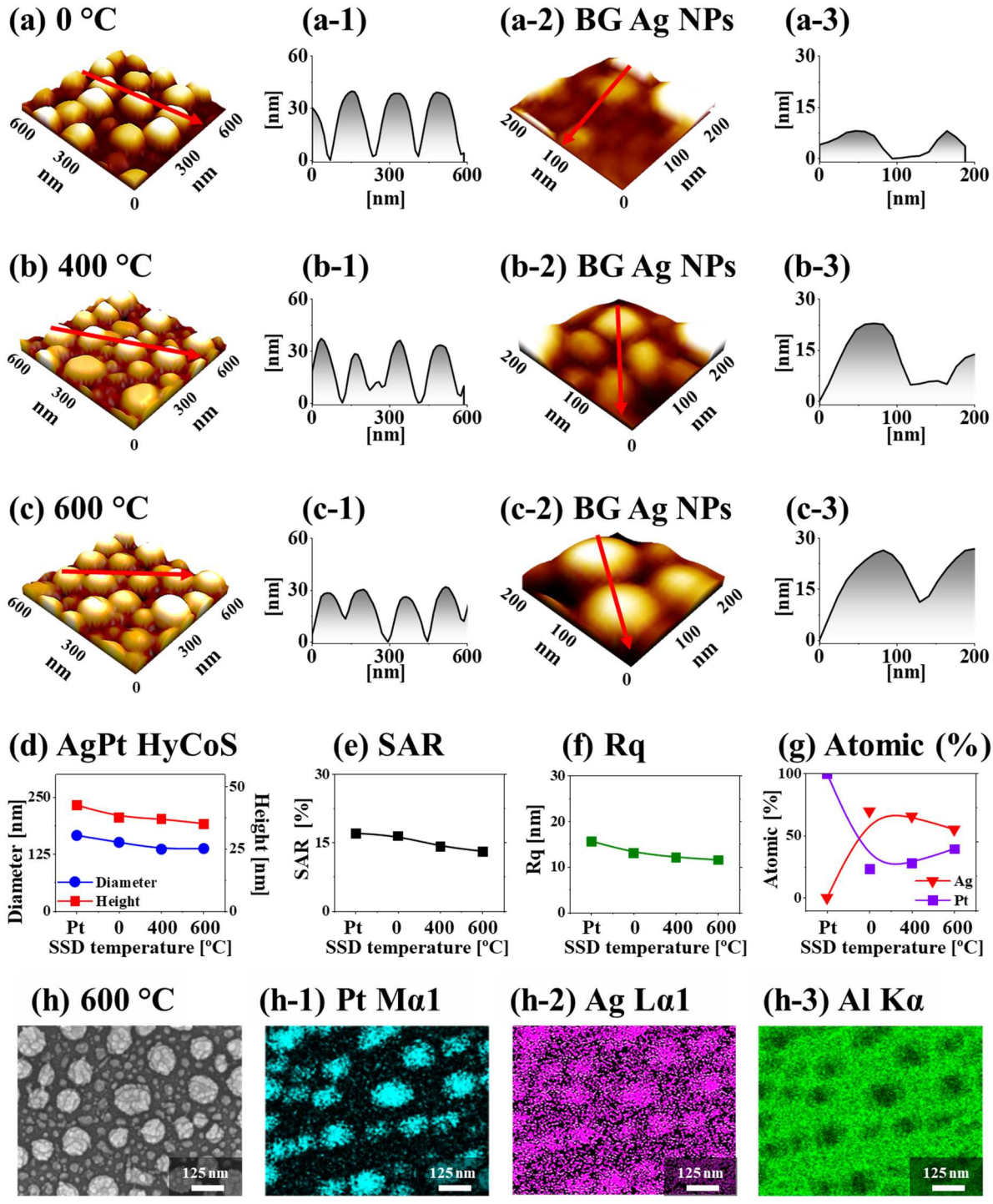

Figure 2: Evolution of AgPt hybrid core-shell (HyCoS) NPs with 10 nm Ag coating on 20 nm Pt NP template. (a) – (c) AFM side-views of AgPt HyCoS NPs. (a-1) – (c-1) Corresponding line-profiles. (a-2) – (c-2) Enlarged side-views of background (BG) Ag NPs. (a-3) – (c-3) Corresponding line-profiles of BG Ag NPs. (d) Summary plots of diameter and height of HyCoS NPs. (e) – (f) Plots of SAR and Rq of samples. (g) Summary of atomic percentage. (h) – (h-3) EDS elemental phase maps of AgPt NPs at 600 °C.

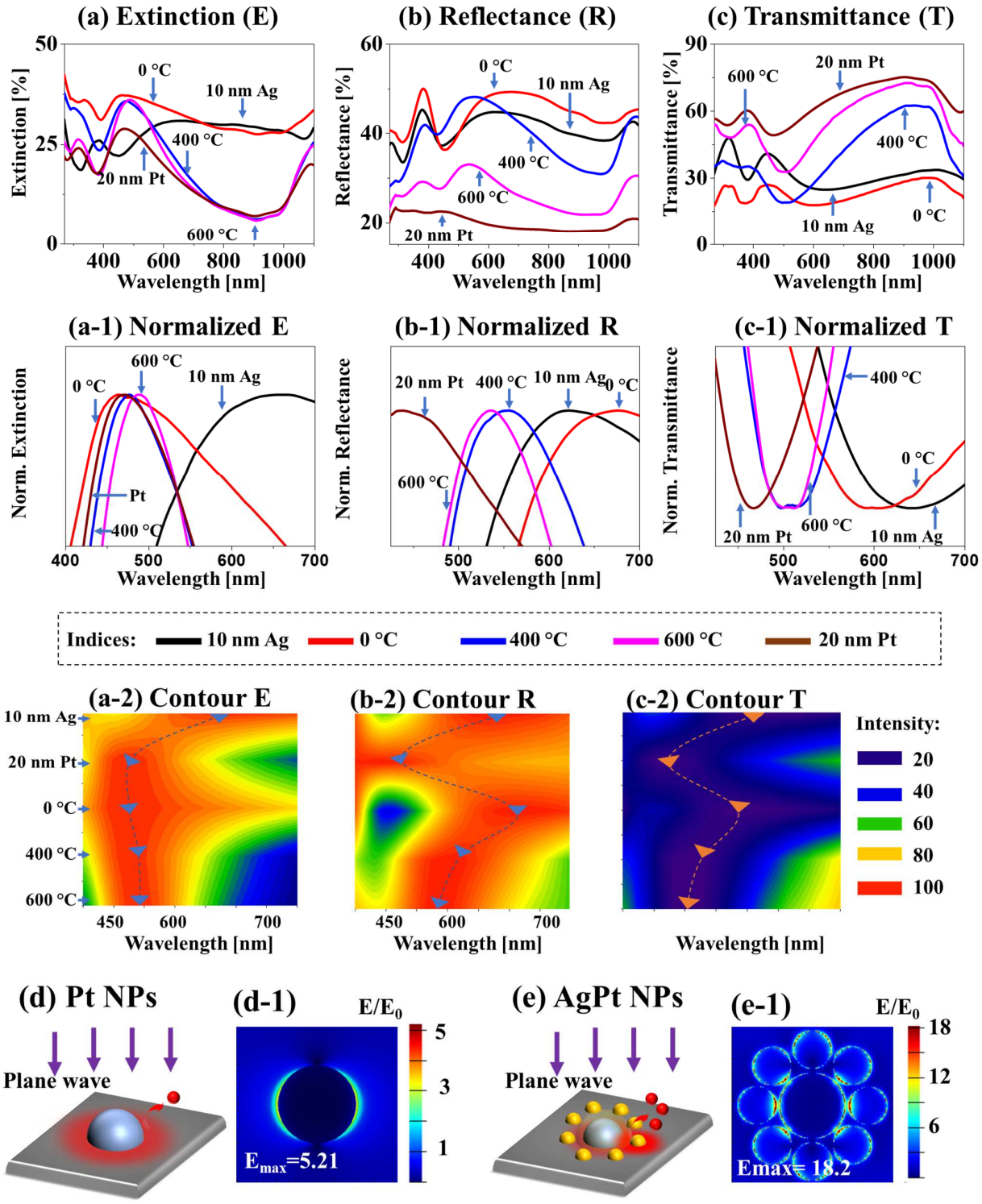

Figure 3: Optical properties of HyCoS AgPt NPs with the 10 nm Ag coatings on the 20 nm Pt templates at different annealing temperatures. (a) – (c) Extinction (E), reflectance (R) and transmittance (T) (ERT) spectra in 270 - 1100 nm region. (a-1) – (c-1) Corresponding normalized spectra. (a-2) – (c-2) Contour plots showing the shift in the peak position. (d) – (e) Schematic representation of FDTD simulation structure for pure Pt and AgPt NPs. (d-1) – (e-1) Top-view of e-field distributions.

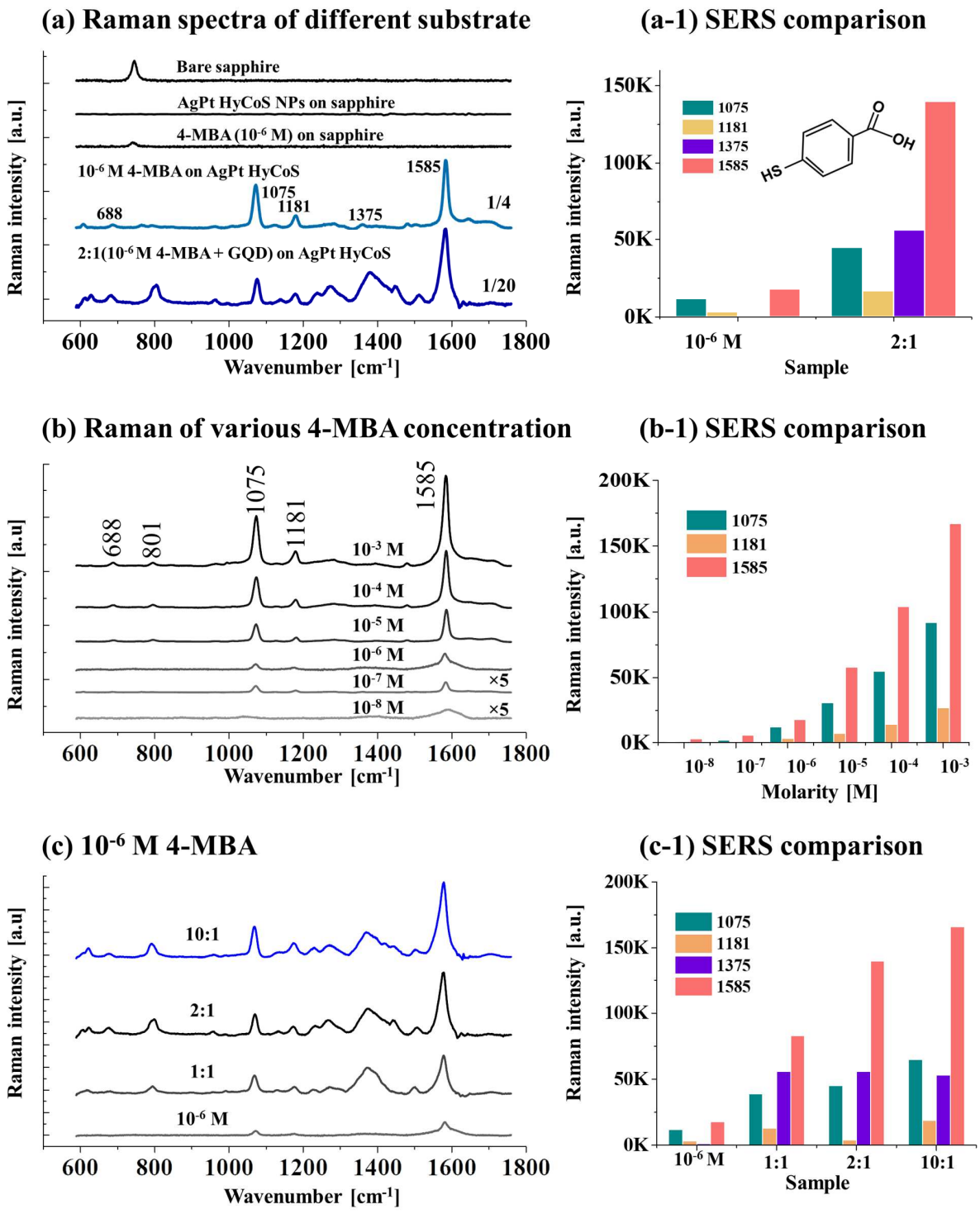

Figure 4: (a) Raman spectra of samples as labelled. (b) SERS spectra of 10^{-8} ~ 10^{-3} M 4-MBA on AgPt NPs. (c) SERS signals of various mixture ratio of 4-MBA and GQD at the 10^{-6} M 4-MBA. (a-1) – (c-1) Bar diagram summary of characteristic peaks.

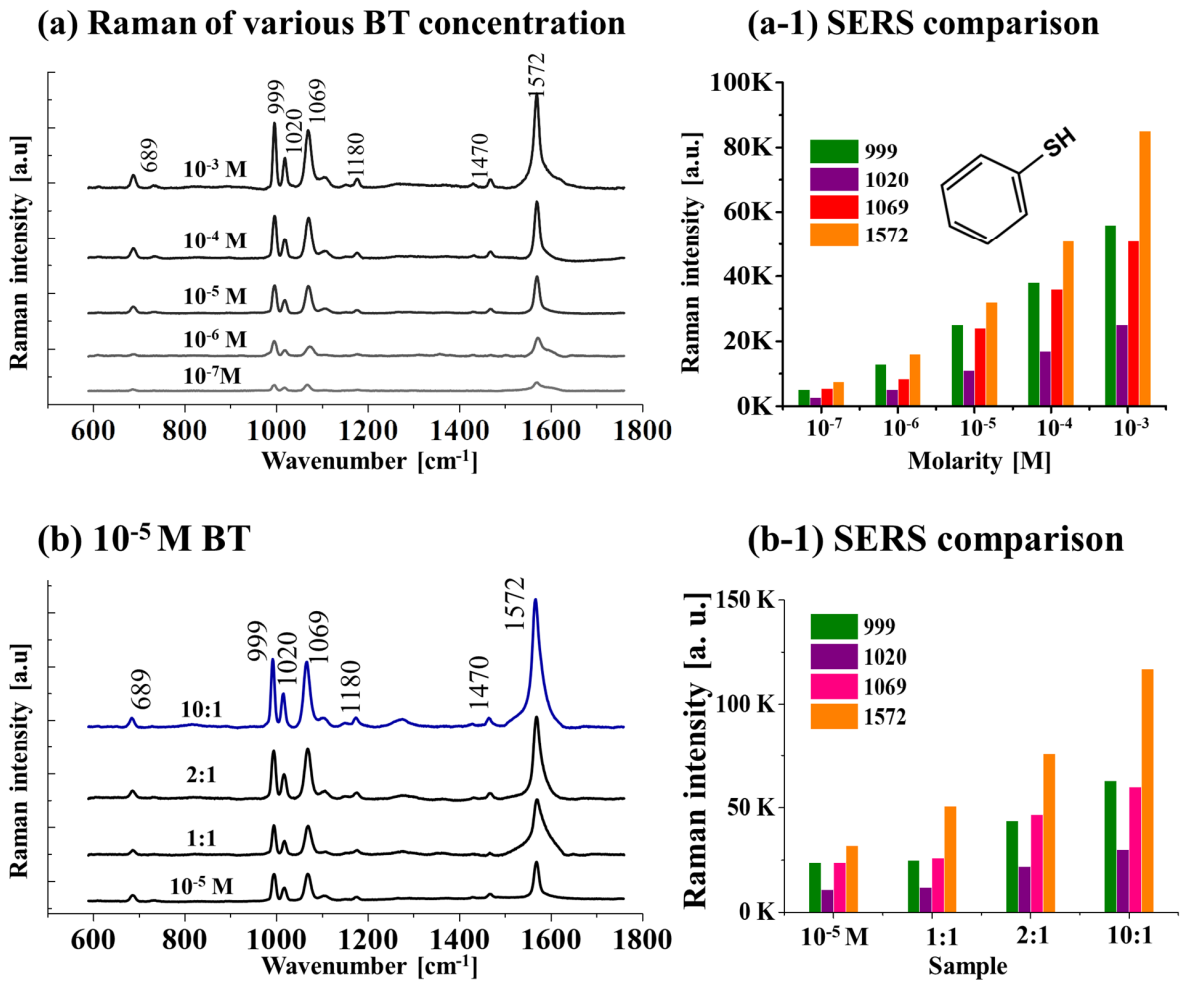

Figure 5: (a) SERS spectra of 10^{-7} ~ 10^{-3} M of benzenethiol (BT) on the HyCoS AgPt NPs. (b) SERS signals of various mixture ratio of BT and GQD at the 10^{-5} M BT. (a-1) – (b-1) Bar diagram of SERS comparison.

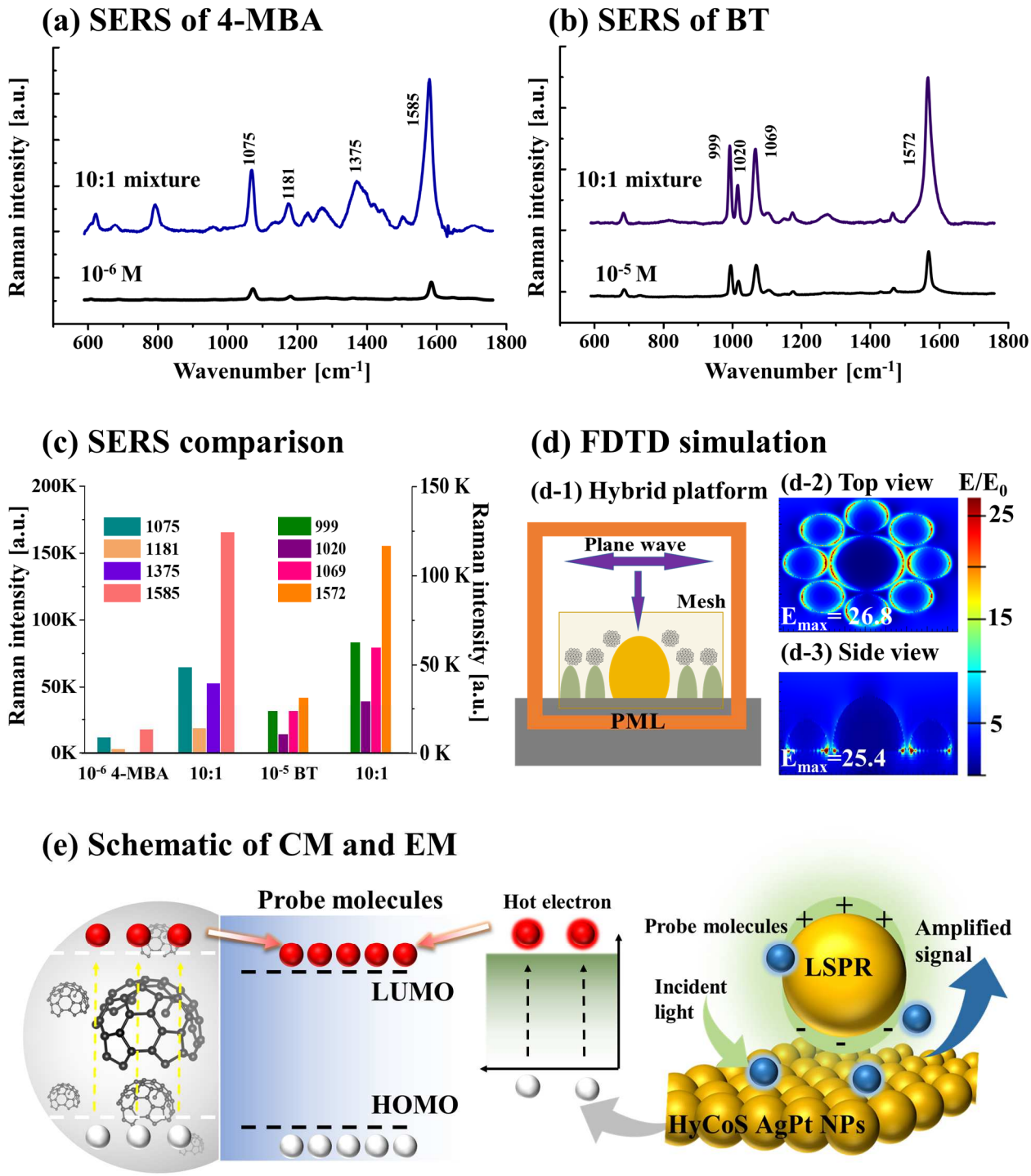

Figure 6: (a) – (b) Summary plot of mixture approach with GQD for 4-MBA and BT. (c) Corresponding bar diagram summary. (d-1) Schematic of FDTD simulation for hybrid GQD/HyCoS AgPt NP architecture. (d-2) – (d-3) Top- and side-views of e-field distributions. (e) Schematic of chemical mechanism (CM), electron plasmon excitation and electromagnetic mechanism (EM).

Graphical abstract

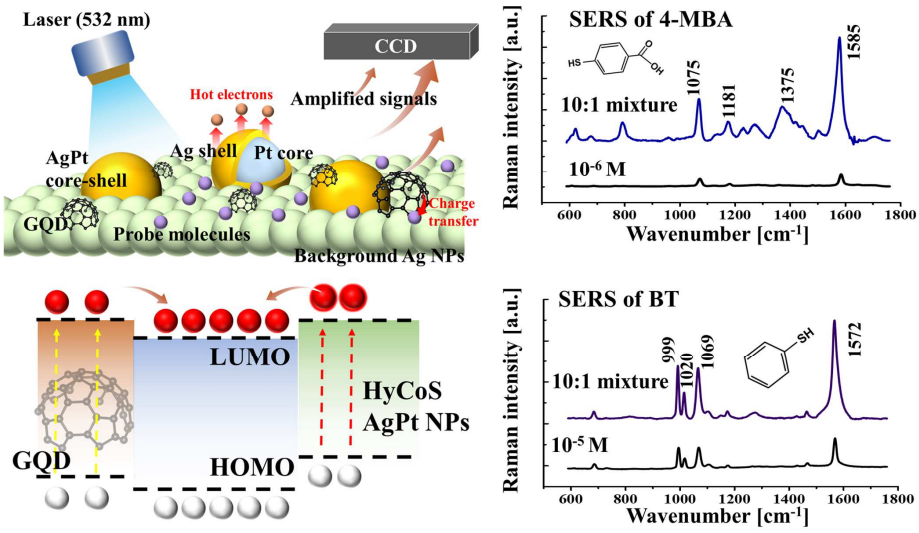

Hybrid SERS platform incorporating plasmonic AgPt hybrid core-shell (HyCoS) NPs and GQD embedded with the probe molecules such as 4-MBA and BT is demonstrated. The hybrid platform takes advantage of both electromagnetic mechanism (EM) and chemical mechanism (CM) enhancements, exhibiting large enhancement in SERS signlas.

Graphical abstract

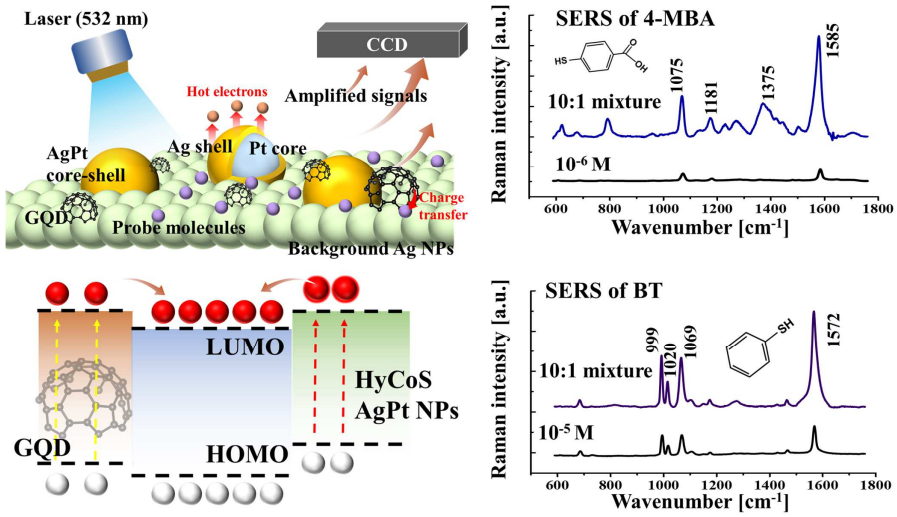

Hybrid SERS platform incorporating plasmonic AgPt hybrid core-shell (HyCoS) NPs and GQD embedded with the probe molecules such as 4-MBA and BT is demonstrated. The hybrid platform takes advantage of both electromagnetic mechanism (EM) and chemical mechanism (CM) enhancements, exhibiting orders of enhancements in SERS signals.